Research Square

Preprints are preliminary reports that have not undergone peer review.
They should not be considered conclusive, used to inform clinical practice,
or referenced by the media as validated information.

CONUS-RecoveryCurves: A dataset of category-specific forest aboveground biomass recovery curves across the conterminous United States

Nan MENG
Laboratoire des Sciences du Climat et de l'Environnement
Yidi Xu
ydxu@des.ecnu.edu.cn

Laboratoire des Sciences du Climat et de l'Environnement
Philippe Ciais
philippe.ciais@lsce.ipsl.fr

Laboratoire des Sciences du Climat et de l'Environnement
Nicolas Viovy
Laboratoire des Sciences du Climat et de l'Environnement
Agnes Pellissier-Tanon
Laboratoire des Sciences du Climat et de l'Environnement

Research Article

Keywords:

Posted Date: November 18th, 2026

DOI: https://doi.org/10.21203/rs.3.rs-11773584/v1

License: This work is licensed under a Creative Commons Attribution 4.0 International License.
Read Full License

Additional Declarations: The authors declare no competing interests.

CONUS-RecoveryCurves: A dataset of category-specific forest aboveground biomass recovery curves across the conterminous United States

Nan Meng[1], Yidi Xu[1,2*], Philippe Ciais[1*], Nicolas Viovy[1], Agnes Pellissier-Tanon[1]

[1] Laboratoire des Sciences du Climat et de l'Environnement, IPSL-LSCE CEA/CNRS/UVSQ, 91190 Gif sur Yvette, France
[2] School of Ecological and Environmental Sciences, East China Normal University, Shanghai, China

[*] Correspondence to Yidi Xu and Philippe Ciais: ydxu@des.ecnu.edu.cn, philippe.ciais@lsce.ipsl.fr

Abstract

Forest biomass recovery curves describe how biomass accumulates with recovery age and provide a basis for quantifying carbon accumulation during forest regrowth. However, spatially explicit biomass recovery-curves that distinguish multiple disturbance types and forest establishment remain limited across the conterminous United States (CONUS). Here, we developed CONUS-RecoveryCurves, a dataset of forest aboveground biomass (AGB) recovery curves at 1° × 1° resolution across the CONUS, based on 1988–2022 event records and covering five recovery categories: fire, wind or geohazard, stress, logging, and afforestation. We corrected ESA CCI AGB using Forest Inventory and Analysis (FIA) observations to reduce regional and age-dependent biases. We then integrated AGB estimates with existing Landsat disturbance histories, land-cover maps, and forest age map to fit Chapman–Richards recovery curves using a space-for-time approach and derive recovery metrics. Using FIA-corrected AGB, valid direct fits were obtained for 47.1%–77.9% of grid cells across the five categories, with median R^2 values of 0.62–0.98. Comparisons with four published datasets showed positive correlations in age–AGB relationships (Pearson's r = 0.80–0.94), whereas comparison with a fifth dataset showed poor agreement in model-derived AGB regrowth rates for 2020. The CONUS-RecoveryCurves dataset provides three main components: an FIA-corrected AGB map, four recovery curve parameters, and three derived recovery metrics, including the estimated AGB at the onset of recovery (*initial AGB*), the maximum recovered aboveground biomass (AGB_{max}), and the average recovery rate over the first 30 years (*R30*), each accompanied by quality layers. CONUS-RecoveryCurves provides baseline data for forest carbon-cycle research, post-disturbance recovery assessment, and terrestrial ecosystem and carbon-cycle model parameterization. The dataset is available at https://figshare.com/s/15137ee983699064574b.

1. Introduction

Forests across the conterminous United States (CONUS) constitute an important carbon sink (Domke et al., 2020), but their carbon storage is influenced by natural disturbances and human activities (Williams et al., 2016; Wu et al., 2026a; Wu et al., 2023). Disturbances alter forest biomass stocks, while subsequent regrowth contributes to carbon accumulation (Williams et al., 2012; Williams et al., 2016). Quantifying post-disturbance biomass recovery is therefore important for assessing disturbance legacies and the contribution of forest regrowth to the carbon sink. Forest biomass recovery curves describe the trajectory of biomass accumulation as forests regrow (Robinson et al., 2025). During recovery, biomass generally increases with age, whereas accumulation rates vary with stand development and decline as biomass approaches its long-term level (Zhu et al., 2018). These curves support forest carbon accounting, help constrain terrestrial biosphere model parameters, and inform assessments of carbon removal potential from forest restoration (Cook-Patton et al., 2020; Wu et al., 2026b; Xu et al., 2026).

Forest biomass recovery varies among disturbance types and across regions. Forests across the CONUS experience different types of disturbances, including fire, wind or geohazard, stress (e.g., pests, pathogens, or drought), and logging (Qiu et al., 2025). Forest establishment following non-forest-to-forest transitions provides an additional context for biomass accumulation (Woodall et al., 2015). Different types of disturbances can lead to contrasting biomass losses and recovery trajectories (Cole et al., 2014; Heinrich et al., 2026). For example, stand-replacing fires combust large amounts of living biomass and leave little surviving vegetation, whereas selective logging and non-stand-replacing wind disturbances may retain varying amounts of vegetation (Frolking et al., 2009; Williams et al., 2016). Even within the same disturbance type, recovery trajectories vary across regions because of differences in climate and forest characteristics. Climate influences early carbon accumulation rates during natural forest regrowth (Cook-Patton et al., 2020), while temperature, precipitation, and forest type also impact long-term biomass accumulation (Zhu et al., 2018). Consequently, average recovery curves may obscure differences among disturbance types and regional variation within each type. Spatially explicit recovery curves that distinguish disturbance types and forest establishment are therefore needed to characterize biomass recovery across the CONUS.

Existing datasets provide valuable information on forest recovery across the CONUS, but vary in the recovery types covered, variables provided, and spatial resolution. Products focused on forest establishment following non-forest-to-forest transitions (Ma & Hurtt, 2026) or post-fire regrowth (Zang et al., 2024) characterize specific recovery contexts, but do not provide comparable trajectories across multiple disturbance types. The National Forest Carbon Monitoring System (NFCMS) provides spatially explicit stand-age and forest carbon-stock estimates following stand-replacing disturbance (Williams et al., 2020), while Robinson et al. (2025) provide recovery-curve parameters for naturally regenerating secondary forests. However, neither product provides separate recovery curves for different recovery categories. Regional

summaries based on Forest Inventory and Analysis (FIA) data further characterize how forest carbon stocks vary with stand age (Hoover & Smith, 2023), but do not resolve recovery trajectories within individual grid cells. A remaining data gap is therefore a consistent set of spatially explicit recovery curves covering multiple disturbance types and forest establishment across the CONUS, derived using a common fitting framework and accompanied by comparable recovery metrics.

Here, we developed CONUS-RecoveryCurves, a spatially explicit dataset of forest aboveground biomass recovery curves at 1° × 1° resolution across the CONUS for five categories: fire, wind or geohazard, stress, logging, and afforestation. We integrated satellite-derived disturbance histories (Qiu et al., 2025), land-cover transitions (https://lcms-viewer.fs2c.usda.gov/), biomass estimates (Santoro & Cartus, 2025), and forest-age maps (Besnard et al., 2021) with FIA observations (Besnard et al., 2021). After calibrating aboveground biomass (AGB) estimates using FIA data, we applied a space-for-time approach to fit Chapman–Richards recovery curves for each category within individual grid cells (Liu & Li, 2003). The dataset provides curve parameters, derived recovery metrics, and associated quality layers, with versions based on both FIA-corrected and original AGB estimates. We assessed the fitted curves through comparisons with published datasets and sensitivity analyses. CONUS-RecoveryCurves is intended to support regional to national assessments of forest recovery and carbon dynamics, as well as the evaluation and parameterization of terrestrial ecosystem models.

2. Methods

2.1 Data sources

We used five main data sources to develop CONUS-RecoveryCurves: LCMS land-cover maps, Landsat-based forest disturbance histories, ESA CCI aboveground biomass (AGB), GAMI forest-age maps, and FIA plot-level age–AGB observations. Five additional published datasets were used for product intercomparison. See below for details.

(1) **LCMS land-cover and land-use data.** The Landscape Change Monitoring System (LCMS; https://lcms-viewer.fs2c.usda.gov/) provides annual 30 m land-cover and land-use maps for the CONUS. We used maps for 1987–2022 to derive annual forest masks and compared consecutive years to identify pixels that changed from non-forest to forest. Only pixels with a single non-forest-to-forest transition and no subsequent reversal during the study period were retained for the afforestation category (**Figure S5f**). The mean annual afforestation area during 1988–2022 was 0.45 ± 0.36 Mha yr^{-1} (mean ± standard deviation across years; **Figure S5a**), close to the 0.40 Mha yr^{-1} reported for the CONUS during 2006–2010 (Harris et al., 2016).

(2) **Landsat forest disturbance data**. The annual 30 m Landsat disturbance dataset developed by Qiu et al. (2025) provides disturbance year and disturbance type across the CONUS for 1988–2022. Four disturbance types relevant to forest recovery were retained: fire, wind or geohazard, stress, and logging. Because the original map includes disturbances on both forest and non-forest land, annual forest masks from LCMS land-cover and land-use data were used to retain only disturbances occurring within forests. Where pixels were identified as both afforestation and forest disturbance, disturbance classification took precedence, and these pixels were excluded from the afforestation category. Mean annual disturbed areas during 1988–2022 were 0.35 ± 0.29 Mha yr^{-1} for fire, 0.05 ± 0.04 Mha yr^{-1} for wind or geohazard, 0.08 ± 0.08 Mha yr^{-1} for stress, and 2.03 ± 0.20 Mha yr^{-1} for logging (mean ± standard deviation across years; **Figure S5a**). The logging and fire estimates were close to the 2.44 and 0.33 Mha yr^{-1}, respectively, reported by Costanza et al. (2023), whereas stress and wind/geohazard estimates were lower than those reported by Harris et al. (2016). These comparisons should be interpreted in light of differences in observation periods and disturbance definitions. Spatial distributions are shown in **Figure S5b–e**.

(3) **ESA CCI AGB data.** The ESA Climate Change Initiative Biomass version 6 product provides global, wall-to-wall AGB estimates at 100 m resolution for multiple epochs, including 2022 (Santoro & Cartus, 2025). The AGB retrieval integrates C-band and L-band synthetic aperture radar observations and is informed by spaceborne lidar measurements of forest structure. The 2022 AGB layer provided the baseline biomass data used for FIA-based calibration and subsequent recovery-curve fitting.

(4) **GAMI forest age data**. The Global Age Mapping Integration version 3.1 product provides global forest stand-age estimates for 2020 at 100 m resolution (Besnard et al., 2021). The product was generated using XGBoost models trained with

forest inventory observations and predictor variables including AGB, canopy height, satellite observations, and climate. In this study, GAMI was used to estimate forest age for pixels without Landsat disturbance records and to identify mature forests used as age–AGB reference points for constraining the long-term recovery curves.

(5) **FIA-derived age-AGB observations.** Plot-level stand-age and AGB observations for the CONUS were obtained from the database compiled by Besnard et al. (2021), which incorporates records from the US Forest Inventory and Analysis program. The retained dataset comprised 373,307 observations from 160,755 unique sites. These observations were matched with ESA CCI AGB to quantify region- and age-specific biases and calibrate the AGB data.

(6) **Published datasets used for product intercomparison**. Five published datasets were used to evaluate CONUS-RecoveryCurves. Ma and Hurtt (2026) provided paired regrowth-age and AGB observations for non-forest-to-forest transitions. NFCMS provided spatially paired stand-age and aboveground woody-carbon estimates (Williams et al., 2020), and Robinson et al. (2025) provided pixel-level Chapman–Richards parameters for naturally regenerating secondary forests. Hoover and Smith (2023) provided FIA-based estimates of aboveground live-tree carbon density by region and stand-age class, from 0–20 years to 121+ years in eastern regions and 300+ years in the Great Plains and western regions. Zang et al. (2024) provided post-fire AGB regrowth rates derived by differentiating regional age–height models combined with height–AGB allometric equations. Their 2020 rate estimates were used for comparison with the corresponding rates derived from our fire recovery curves. Dataset characteristics and comparison methods are summarized in **Table 1**.

Table 1. Characteristics of published datasets used for intercomparison with CONUS-RecoveryCurves.

Compared categories	Recovery context	Available information	Spatial range and resolution	Comparison methods
Afforestation	Forest regrowth following the most recent non-forest-to-forest transitions	Regrowth age derived from annual NLCD land-cover transitions, paired with AGB from ESA CCI grids or GEDI L4A footprints	CONUS; approximately 100-m ESA CCI grids and GEDI L4A footprints	GEDI AGB observations from Ma and Hurtt (2026) were grouped by 1° grid cell and 5-year recovery-age class. For each group, we calculated the median recovery age and median GEDI AGB. Our fitted afforestation curve for the corresponding grid cell was evaluated at that median age, and the resulting AGB estimate was compared with the median GEDI AGB.
Fire and logging	Forest carbon dynamics following stand-replacing harvest and fire disturbances	Stand age derived from NAFD and MTBS disturbance histories or, for forests without recorded stand-clearing disturbance, inferred from NBCD biomass, FIA biomass-accumulation curves, and site productivity; paired with aboveground woody carbon simulated by an inventory-constrained CASA model	CONUS; 30 m	Paired NFCMS stand-age and aboveground woody-carbon estimates for 2010 (Williams et al., 2020) were sampled at approximately 1.2-km intervals, converted to dry AGB using a carbon fraction of 0.5, and summarized by 1° grid cell and 5-year stand-age class. For each group, we calculated the median stand age and median NFCMS AGB. Our fitted fire and logging curves for the corresponding grid cell were evaluated at that median age, and the resulting AGB estimates were compared separately with the median NFCMS AGB. NFCMS samples were not separated by disturbance type, so these comparisons assess overall consistency rather than type-specific agreement.
All five recovery categories	Natural regeneration of secondary forests	Pixel-level Chapman–Richards parameters (A, B, and K)	Global; 30 arcsec (approximately 1 km at the	AGC at 5-year intervals from ages 5 to 100 years was reconstructed using the approximately 1-km curve parameters published by Robinson et al. (2025). After conversion to AGB, estimates were aggregated to the

			Equator)	median within each 1° grid cell at each age and compared with the corresponding age-specific AGB estimates from our five recovery categories. The reference curves do not distinguish disturbance types; comparisons therefore assess consistency in age–AGB relationships rather than category-specific agreement.
All five recovery categories	Age-related forest carbon dynamics	Aboveground live-tree carbon density by region and stand-age class	CONUS; FIA regional and stand-age-class summaries	For each recovery category, AGB was calculated from the fitted curves at each integer age within each stand-age class. Estimates were then averaged across these ages and the valid 1° grid cells within each corresponding FIA region, and compared with the regional age-class AGB estimates from Hoover and Smith (2023). All five recovery categories were compared separately with the same regional age-class reference estimates, which were not differentiated by recovery category.
Fire	Forest regrowth following wildfires	AGB regrowth rates for 2020 derived by differentiating regional age–height models combined with height–AGB allometric equations.	Global; 30 m	Zang et al. (2024) provide model-derived AGB regrowth rates for 2020. Corresponding rates were calculated from the derivatives of our fire recovery curves at each pixel's recovery age in 2020. Both products were expressed in Mg ha^{-1} yr^{-1}, and median rates were calculated over common valid pixels with positive rates in both products within each 1° grid cell for comparison.

2.2 Methodological framework

The workflow for generating CONUS-RecoveryCurves consists of six steps: spatial harmonization, recovery-age estimation, AGB bias correction, recovery-curve fitting and metric derivation, quality-layer generation and product intercomparison, and dataset assembly (**Figure 1**). These steps are described below.

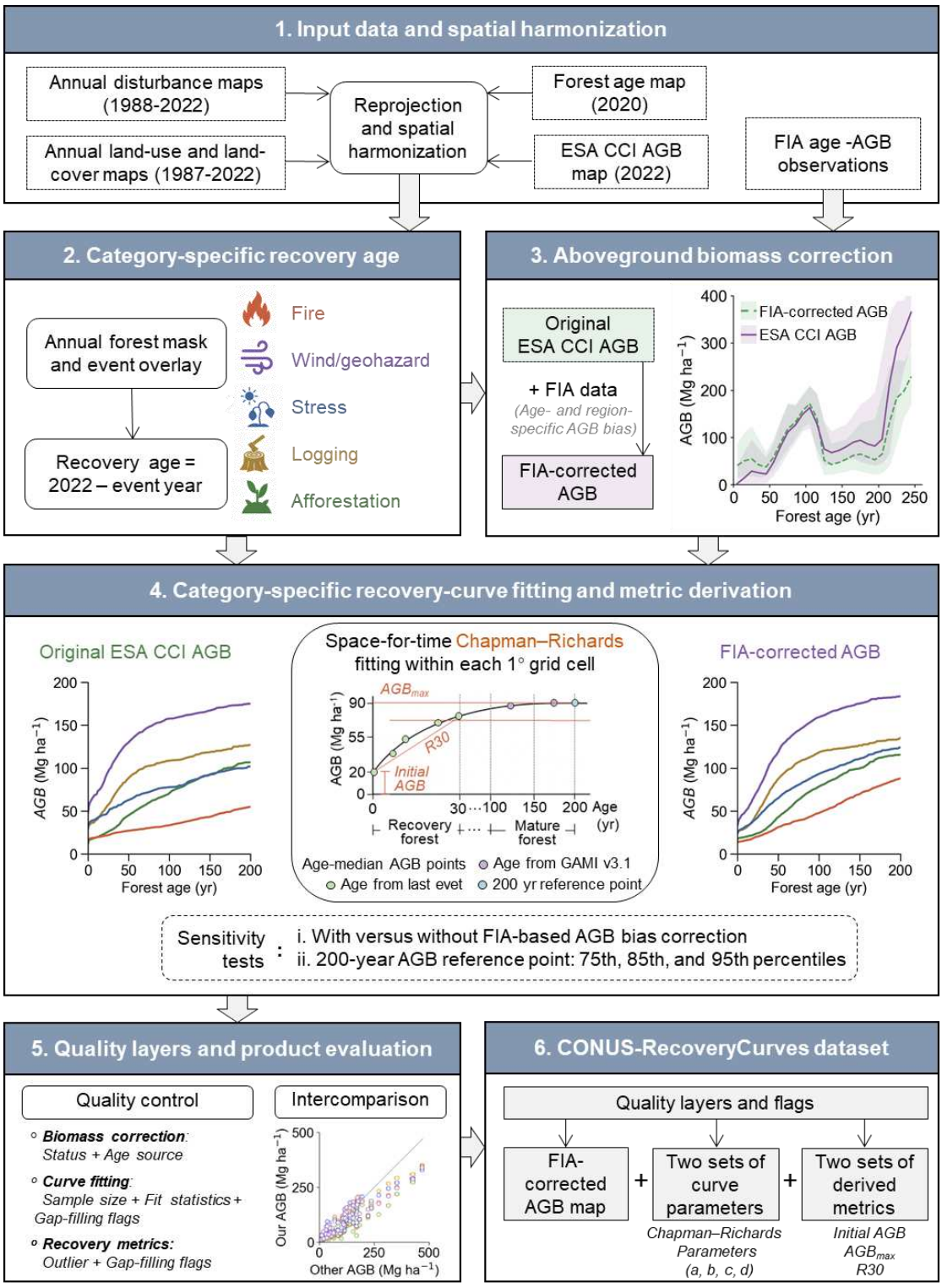


Figure 1. Workflow for generating the CONUS-RecoveryCurves dataset. The

workflow includes input data integration, recovery-age estimation, FIA-based AGB calibration, recovery-curve fitting, sensitivity analyses, and the resulting data products.

(1) **Input data and spatial harmonization**. The datasets described in **Section 2.1** were combined to identify recovery categories, estimate recovery ages, calibrate AGB, and fit recovery curves. All spatial raster datasets were aligned to a common grid in the WGS 84 geographic coordinate system (EPSG:4326), with a pixel spacing of 0.00025°.

(2) **Category-specific recovery age**. We considered five recovery categories: fire, wind or geohazard, stress, logging, and afforestation. Each pixel was assigned to the category of its most recent disturbance or forest-establishment event during 1988–2022. Recovery age was calculated as 2022 minus the year of that event.

(3) **FIA-based AGB bias correction**. Comparison with FIA data (Besnard et al., 2021) showed that ESA CCI AGB systematically overestimated AGB in young, low-biomass forests and underestimated it in older, high-biomass forests across CONUS (**Figure S1**). We therefore corrected ESA CCI AGB using spatially matched FIA age–AGB records. FIA records were grouped into nine stand-age classes (<20, 20–40, 40–60, 60–80, 80–100, 100–150, 150–200, 200–250, and ≥250 years) within each of ten forest regions based on Smith et al. (2006). For each region and age class, we calculated the median CCI−FIA difference, first taking the median of repeated observations at each coordinate. Missing regional age-class biases were replaced by the corresponding CONUS-wide median. These age-class biases were linearly interpolated between representative ages to obtain region- and age-specific biases for integer ages from 0 to 300 years. Each eligible ESA CCI AGB pixel was corrected according to its region and estimated forest age in 2022 using **Eq. (1)**. Forest age was derived from the most recent recorded disturbance or forest-establishment event where available; otherwise, GAMI forest age for 2020 was increased by two years. Pixels lacking usable age information retained their original ESA CCI AGB values.

$$AGB_{cal} = \max(0, AGB_{CCI} - Bias_{r,g}) \quad (1)$$

where $Bias_{r,g}$ is the interpolated CCI−FIA AGB difference for forest region r and pixel age g.

(4) **Category-specific recovery-curve fitting, metric derivation, and sensitivity experiments**. We applied a space-for-time substitution approach to fit forest biomass recovery curves (Xu et al., 2026). For forests experiencing disturbance or afforestation during 1988-2022, recovery age was calculated as 2022 minus the year of the most recent event. GAMI forest ages (Besnard et al., 2021) were used to identify mature forests in the 100–150- and 150–200-year age classes. Each pixel's recovery age or mature-forest age class was paired with its corresponding AGB estimate for 2022. Within each 1° × 1° grid cell, median AGB was calculated for each recovery age separately for each recovery category, and for each mature-forest age class. Where no reference point aged ≥200 years was available, a 200-year reference point was assigned

using the 85th percentile of AGB from forests with no recorded disturbance within the same grid cell. These mature-forest reference points were combined with the recovery-stage age–AGB pairs to fit the Chapman–Richards recovery curves for each recovery category within each 1° × 1° grid cell (Liu & Li, 2003), yielding four parameters (a, b, c, and d) (**Eq. (2)**). Three recovery metrics, including the estimated AGB at the onset of recovery (*initial AGB*), the maximum recovered aboveground biomass (AGB_{max}), and the average recovery rate over the first 30 years (*R30*) were then derived from the fitted curves. Approximate standard errors were estimated to quantify fitting uncertainty in the four curve parameters and three derived recovery metrics. Approximate standard errors of the fitted parameters were obtained from the estimated covariance matrix of the nonlinear least-squares fit (Bates & Watts, 1988). Approximate standard errors of the derived recovery metrics were then approximated using the delta method (Oehlert, 1992), accounting for covariance among the fitted parameters.

$$AGB_t = a \times (1 - e^{-bt})^c + d \quad (2)$$

where t is recovery age, d is *initial AGB* at t=0, a is the recoverable AGB increment above *initial AGB*, and b and c are the rate and shape parameters, respectively.

We conducted two sensitivity tests using FIA-corrected AGB and the 85th-percentile 200-year reference point as the baseline configuration. In the reference point sensitivity test (Test S1), we assessed the effect of reference point selection by comparing the 75th- and 95th-percentile configurations with the 85th-percentile baseline, using FIA-corrected AGB throughout. In the AGB correction sensitivity test (Test S2), we assessed the effect of AGB bias correction by comparing recovery curves fitted using original ESA CCI AGB with those fitted using FIA-corrected AGB, retaining the 85th-percentile reference point specification in both configurations. All other input data and curve-fitting procedures were unchanged. For each recovery category, sensitivity was quantified as the relative change in the median *initial AGB*, AGB_{max}, and *R30* across matched grid cells (**Eq. (3)**):

$$\Delta M = \frac{M_{alternative} - M_{reference}}{M_{reference}} \times 100 \quad (3)$$

where $M_{alternative}$ and $M_{reference}$ are the medians of *initial AGB*, AGB_{max}, or *R30* across matched grid cells within each recovery category under the alternative and baseline configurations, respectively. The AGB bias-correction comparison used valid direct-fit grids shared by the original and FIA-corrected AGB configurations; the reference point comparisons used those shared by all three percentile configurations. Gap-filled estimates were excluded. Paired-grid bootstrap resampling with 2,000 iterations provided 95% intervals based on the 2.5th and 97.5th percentiles, representing grid-level sampling variability.

(5) **Quality layers and intercomparison with published datasets.** Quality layers were provided for the FIA-corrected AGB map, recovery-curve parameters, and derived recovery metrics. For AGB bias correction, we recorded the correction status and forest-age source. For curve fitting, we recorded the number of fitting points, including recovery-stage age–median AGB pairs and mature-forest reference points, together with fitting statistics (R^2 and RMSE). Fits with non-positive R^2 or biologically implausible estimates of asymptotic biomass or recovery duration were classified as invalid. Grid cells without valid fits were gap-filled using the nearby recovery curves, and the gap-filled cells were identified using quality-control flags. For recovery metrics, similarly, we gap-filled the grids without successive fits using the metrics from the nearby curves. Quality layers for curves and metrics was conducted separately for the original and FIA-corrected AGB versions (**Table 2**).

To assess the consistency of CONUS-RecoveryCurves with existing recovery estimates, we compared with five published datasets. Because these datasets differ in recovery context, available variables, and spatial and temporal scales, each dataset was processed separately to match the most comparable recovery variable and scale in CONUS-RecoveryCurves (**Table 1**).

(6) **The CONUS-RecoveryCurves dataset**. The final dataset includes three main components: an FIA-corrected AGB map, Chapman–Richards curve parameters (a, b, c, and d), and derived recovery metrics (*initial AGB*, AGB_{max}, and *R30*), each accompanied by quality layers. Curve parameters, recovery metrics, and quality layers were provided separately for the five recovery categories and for versions based on original ESA CCI AGB and FIA-corrected AGB. **Table 2** summarizes the dataset components and variables, including their definitions, units, and spatial resolutions.

3. Data records

CONUS-RecoveryCurves comprises three main components: an FIA-corrected AGB map, category-specific recovery-curve parameters, and derived recovery metrics, each accompanied by quality layers. Curve parameters, recovery metrics, and their quality layers are provided separately for five recovery categories and two AGB versions: original ESA CCI and FIA-corrected AGB. **Table 2** summarizes the dataset components, variables, descriptions, units, and spatial resolutions. All data files and accompanying metadata are publicly available from Figshare at https://figshare.com/s/15137ee983699064574b.

Table 2. Components and variables of the CONUS-RecoveryCurves dataset. Curve parameters, recovery metrics, and their quality layers are provided separately for five recovery categories and two AGB versions: original ESA CCI AGB and FIA-corrected AGB.

Component		Variable	Description	Unit	Spatial resolution
FIA-corrected AGB map		FIA-corrected AGB	ESA CCI AGB corrected using FIA observations for 2022	Mg ha^{-1}	0.00025°
Recovery-curve parameters		*a*	Recoverable AGB increment above initial AGB	Mg ha^{-1}	1°
		b	Rate parameter of the Chapman–Richards function	yr^{-1}	1°
		c	Shape parameter of the Chapman–Richards function	Dimensionless	1°
		d	Initial AGB	Mg ha^{-1}	1°
Derived recovery metrics		*Initial AGB*	The estimated AGB at the onset of recovery, equal to *d* in Chapman–Richards function	Mg ha^{-1}	1°
		AGB_{max}	The maximum recovered aboveground biomass AGB, equal to *a* + *d* in Chapman–Richards function	Mg ha^{-1}	1°
		R30	The average recovery rate over the first 30 years	Mg ha^{-1} yr^{-1}	1°
Quality layers	FIA-corrected AGB map	AGB calibration flag	AGB calibration status and age source: 1, corrected using Landsat-derived event age; 2, corrected using GAMI-derived forest age; 3, original CCI AGB retained without correction; 255, NoData.	Categorical	0.00025°
	Recovery-curve parameters	Number of fitting points	Number of age–AGB points used for curve fitting, including recovery-stage age–median AGB points, mature-forest reference points, and the 200-year reference point where included.	Count	1°
		R^2	Coefficient of determination for curve fitting	Dimensionless	1°
		RMSE	Root mean square error of curve fitting	Mg ha^{-1}	1°

	Gap-filling flag	Curve estimation status: 1, valid direct fit; 2, spatially gap-filled estimate; 255, NoData.	Categorical	1°
	Approximate standard errors	Approximate standard errors of the four curve parameters (*a*, *b*, *c*, and *d*).	Same as corresponding parameter	1°
Derived recovery metrics	Gap-filling flag	Metric provenance: 1, derived from a valid direct fit; 2, derived from a spatially gap-filled curve; 255, NoData.	Categorical	1°
	Approximate standard errors	Approximate standard errors of *initial AGB*, AGB_{max}, and *R30,* estimated using the delta method.	Same as corresponding metric	1°

115

4. Technical validation and product characteristics

4.1 AGB bias-correction assessment

Comparison with FIA data indicated that ESA CCI AGB was generally higher than FIA AGB in younger forests and lower in older forests (**Figure S1**). FIA-based bias correction therefore reduced AGB in younger age classes and increased it in older age classes. Median AGB in the 20–30-year age class decreased from 55.0 to 29.1 Mg ha^{-1}, a reduction of 47.1%. Between 60 and 120 years, median AGB values before and after correction remained similar, with absolute relative differences below 10% in all age classes within this range. Older age classes, by contrast, showed increases after correction. For example, median AGB in the 230–240-year age class increased from 198.0 to 324.6 Mg ha^{-1}, a relative increase of 63.9% (**Figure 2a**). These age-class medians summarize different forest pixels rather than fitted recovery trajectories. Their non-monotonic pattern partly reflects changes in regional sample composition across age classes (**Figure S6**). Spatial comparisons of AGB at the 1° × 1° grid-cell scale indicated that FIA-corrected AGB was higher than original ESA CCI AGB in parts of the western CONUS and lower across several eastern regions (**Figure 2b**).

The effects of FIA-based bias correction varied by region and forest age (**Figure 3**). In most western regions, correction reduced AGB overestimation in young forests and underestimation in mature forests. For example, median biases generally moved closer to zero across age classes in PWW, PWE, and PSW (**Figure 3a-c**). Correction effects were more variable within the eastern CONUS. In the northern Lake States and northeastern regions, NLS and NE (**Figure 3g-h**), overestimation in young forests decreased substantially, although positive biases remained in some mature-forest age classes. In the southeastern regions, SE and SC (**Figure 3i-j**), improvements were concentrated in the 0–20-year age class, whereas underestimation increased in the 20–35-year age class and overestimation in mature forests did not improve.

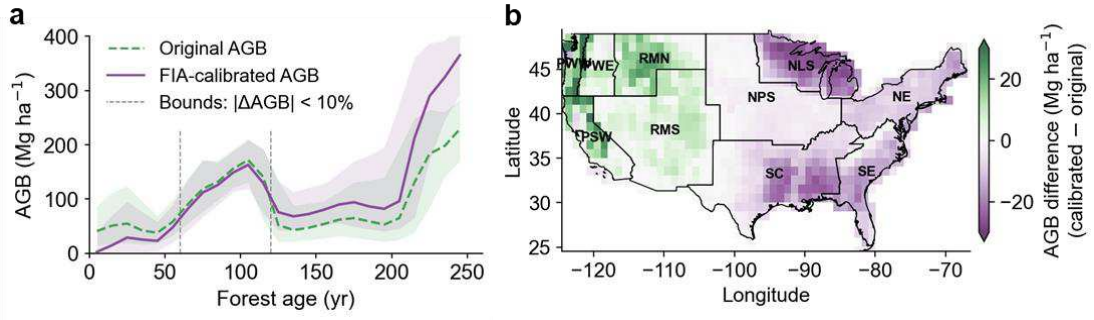


Figure 2. Effects of FIA-based AGB bias correction. a, Median original and FIA-corrected AGB within 10-year forest-age classes across the CONUS. Shading represents the 25th–75th percentiles of sampled pixel-level AGB within each age class. Vertical dashed lines delimit the age classes for which the absolute difference between corrected and original median AGB is less than 10% of the original median. **b**, Difference between FIA-corrected and original mean AGB within each 1° × 1° grid cell, calculated as corrected minus original AGB. Regional abbreviations: PWW, Pacific

Northwest, West; PWE, Pacific Northwest, East; PSW, Pacific Southwest; RMN, Rocky Mountain, North; RMS, Rocky Mountain, South; NPS, Northern Prairie States; NLS, Northern Lake States; NE, Northeast; SC, South Central; SE, Southeast.

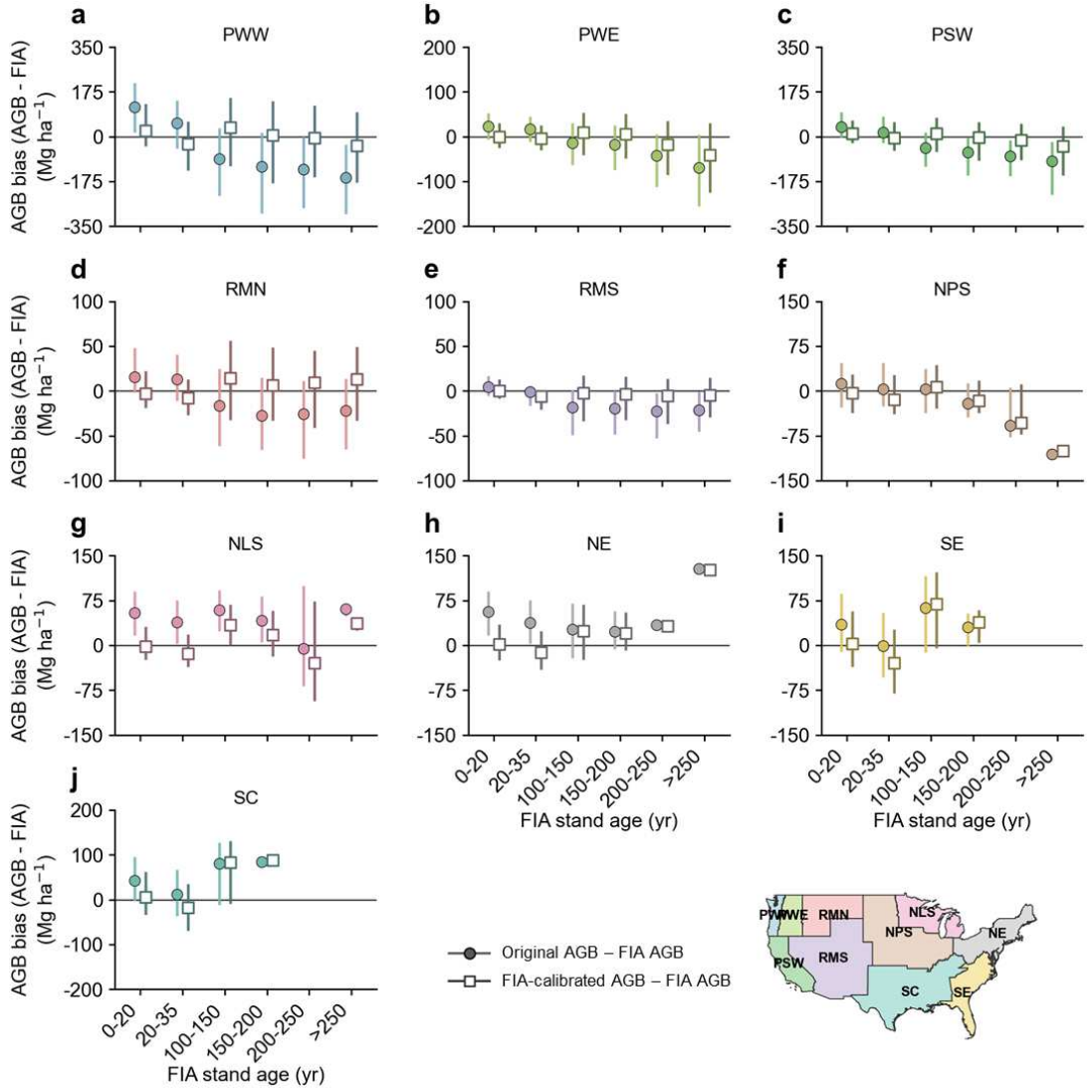


Figure 3. Regional AGB biases before and after FIA-based correction. a-j, Median AGB biases (ESA CCI AGB minus FIA AGB) before and after correction across ten forest regions defined by Smith et al. (2006) and FIA stand-age information (Besnard et al., 2021). Circles and squares represent original ESA CCI AGB and FIA-corrected AGB, respectively; vertical bars indicate the interquartile range. Regional abbreviations: PWW, Pacific Northwest, West; PWE, Pacific Northwest, East; PSW, Pacific Southwest; RMN, Rocky Mountain, North; RMS, Rocky Mountain, South; NPS, Northern Prairie States; NLS, Northern Lake States; NE, Northeast; SC, South Central; SE, Southeast.

4.2 Recovery curves and fitting performance

Figure 4a presents an example of recovery curve following fires fitted within a 1° × 1° grid cell. This fitted recovery curve captured the age–AGB relationship well, with an R^2 of 0.83 and an RMSE of 9.83 Mg ha^{-1}. Additional examples illustrate contrasting

recovery trajectories for fire in southwestern Oregon, logging in southeastern Georgia, and stress in California's Sierra Nevada (**Figure 4c**). Background information on these disturbance contexts is summarized in **Table S2**. Applying this approach to 1° × 1° grid cells across the CONUS yielded spatially explicit recovery-curve parameters for each category, summarized as CONUS-wide recovery trajectories in **Figure 4b**. Regional summaries showed substantial variation within each recovery category, with higher predicted AGB in PWW than in RMS across all five categories at older forest ages (**Figure S4**). The CONUS-wide median trajectories also differed among the five categories. At a recovery age of 60 years, median predicted AGB was 133.4 Mg ha^{-1} for wind/geohazard and 100.8 Mg ha^{-1} for logging, compared with 35.7 Mg ha^{-1} for fire. These contrasts reflect not only differences among recovery categories but also the geographic and environmental distributions of the grid cells in which they occur. For example, fire-affected grid cells are concentrated largely in the western CONUS, whereas logging is more prevalent in the Southeast, where climatic and forest conditions generally support higher biomass (**Figure S5**).

The fitting performance also varied across region and recovery category (**Table 3**; **Figure S2**). Afforestation showed the highest goodness of fit (median R^2 = 0.98, IQR: 0.95–0.99) and lowest fitting error (median RMSE = 3.2 Mg ha^{-1}, IQR: 1.7–5.1 Mg ha^{-1}), followed by logging (median R^2 = 0.90; median RMSE = 7.8 Mg ha^{-1}). Fire, wind/geohazard, and stress had lower median R^2 values (0.62–0.78) and higher median RMSE values (10.3–24.7 Mg ha^{-1}). The proportion of grid cells with valid direct fits was 77.9% for afforestation, 75.7% for logging, 56.3% for stress, 49.5% for fire, and 47.1% for wind/geohazard. Spatially, fire generally showed higher R^2 in western regions and lower R^2 in parts of RMS and SE, whereas logging showed higher R^2 in SC and SE and lower values in parts of RMS and NPS (**Figure S2**).

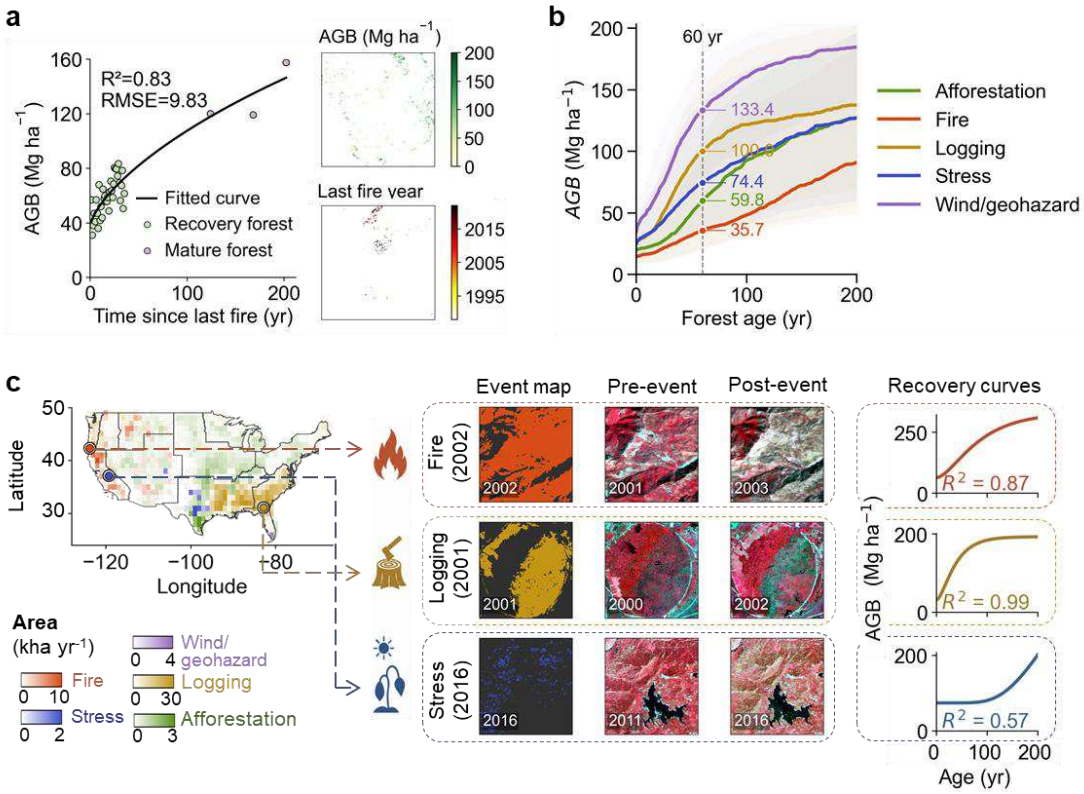


Figure 4. Example of the curve fitting and CONUS-wide recovery trajectories based on FIA-corrected AGB. **a**, Representative example of a fire recovery curve fitted using the Chapman–Richards function. **b**, CONUS-wide recovery trajectories for five recovery categories. Solid lines show the median AGB across directly fitted 1° × 1° grid cells at each recovery age, and shading indicates the corresponding interquartile range. **c**, Spatial distribution of the dominant recovery category, determined by the largest mean annual area within each grid cell; color intensity represents that category's mean annual area. Marked locations identify fire, logging, and stress examples, with event maps, pre- and post-event imagery, and corresponding recovery curves. Curves represent category-specific estimates for the containing 1° × 1° grid cells, rather than observed time series for the illustrated event patches.

Table 3. Performance and coverage of recovery curves fitted using FIA-corrected AGB for five recovery categories. Corresponding results for curves fitted using original ESA CCI AGB are provided in **Table S1**

Type	R^2 (Median; IQR)	RMSE (Mg ha^{-1}) (Median; IQR)	Fitted grids (%)
Fire	0.78 (0.59–0.90)	10.3 (5.4–21.5)	49.5
Wind/geohazard	0.67 (0.51–0.82)	24.7 (15.8–35.0)	47.1
Stress	0.62 (0.48–0.77)	18.9 (8.9–30.6)	56.3
Logging	0.90 (0.71–0.96)	7.8 (4.8–13.0)	75.7
Afforestation	0.98 (0.95–0.99)	3.2 (1.7–5.1)	77.9

4.3 Derived recovery metrics

The derived recovery metrics varied among recovery categories and across the CONUS (**Fig. 5**). Across categories, median *initial AGB* ranged from 12.2 Mg ha^{-1} for fire to 22.5 Mg ha^{-1} for wind/geohazard, while median AGB_{max} ranged from 102.7 to 158.6 Mg ha^{-1} for these two categories, respectively (**Fig. 5a, b**). Median *R30* ranged from 0.20 Mg ha^{-1} yr^{-1} for fire to 0.86 Mg ha^{-1} yr^{-1} for wind/geohazard, with substantial variation among 1° × 1° grid cells within each category (**Fig. 5c**). Spatially, *initial AGB* and AGB_{max} were generally higher in the eastern and southeastern CONUS and parts of the Pacific Northwest than in the interior western regions. Higher *R30* values for logging, stress, and wind/geohazard occurred mainly in the eastern and southeastern CONUS, whereas fire and afforestation generally showed lower and more spatially heterogeneous rates (**Fig. 5d–r**).

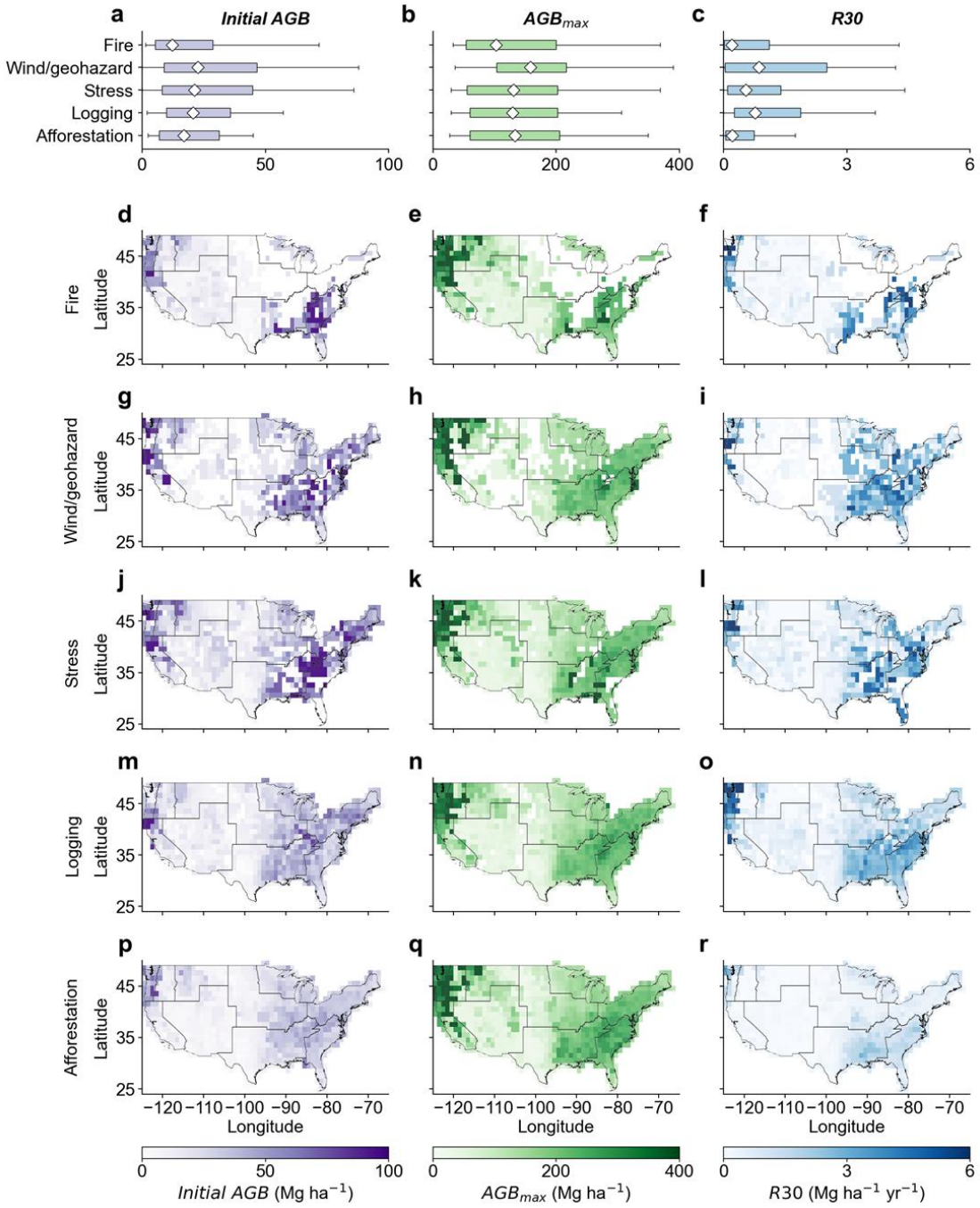


Figure 5. Recovery metrics across five recovery categories based on FIA-corrected AGB. **a-c**, Distributions of the estimated AGB at the onset of recovery (*initial AGB*), the maximum recovered aboveground biomass (AGB_{max}), and the average recovery rate over the first 30 years (*R30*) across 1° × 1° grid cells. Boxes represent the interquartile range, whiskers represent the 5th–95th percentile range, and white diamonds indicate the median. **d-r**, Spatial distributions of the corresponding metrics for fire, wind/geohazard, stress, logging, and afforestation. Values are shown for grid cells containing the corresponding recovery category; estimates for cells without valid direct fits were obtained through gap filling using the nearby curves. Grid cells without colored values indicate that no corresponding disturbance or forest-establishment event was identified in the input datasets within that grid cell.

4.4 Intercomparison with published datasets

We compared CONUS-RecoveryCurves with five published datasets using matched recovery variables and spatial and age scales where possible (**Figure 6**). Afforestation curves were strongly correlated with the age-matched GEDI AGB estimates (Ma & Hurtt, 2026) (r = 0.83; RMSE = 52.7 Mg ha^{-1}), but generally predicted lower AGB (**Figure 6a**). Comparisons with NFCMS estimates from Williams et al. (2020) yielded correlations of 0.80 and 0.81 for fire and logging, respectively, with corresponding RMSE values of 61.4 and 48.2 Mg ha^{-1} (**Figure 6b**). Across the five recovery categories, comparisons with Robinson et al. (2025) yielded correlations of 0.80–0.90 and RMSE values of 29.2–43.6 Mg ha^{-1} (**Figure 6d**). Comparisons with the regional age-class estimates of Hoover and Smith (2023) yielded correlations of 0.91–0.94 and RMSE values of 43.1–61.9 Mg ha^{-1} (**Figure 6e**). These positive correlations indicate consistency in broad age–AGB patterns, although differences in AGB magnitude remained. Differences in data sources, carbon-to-biomass conversion, and spatial aggregation may contribute to these discrepancies (**Table 1**). In contrast, comparison with Zang et al. (2024) showed poor agreement in model-derived AGB regrowth rates for 2020 (r = -0.16; RMSE = 4.91 Mg ha^{-1} yr^{-1}; **Figure 6c**). Differences in model formulation and recovery-age estimates may contribute to this discrepancy.

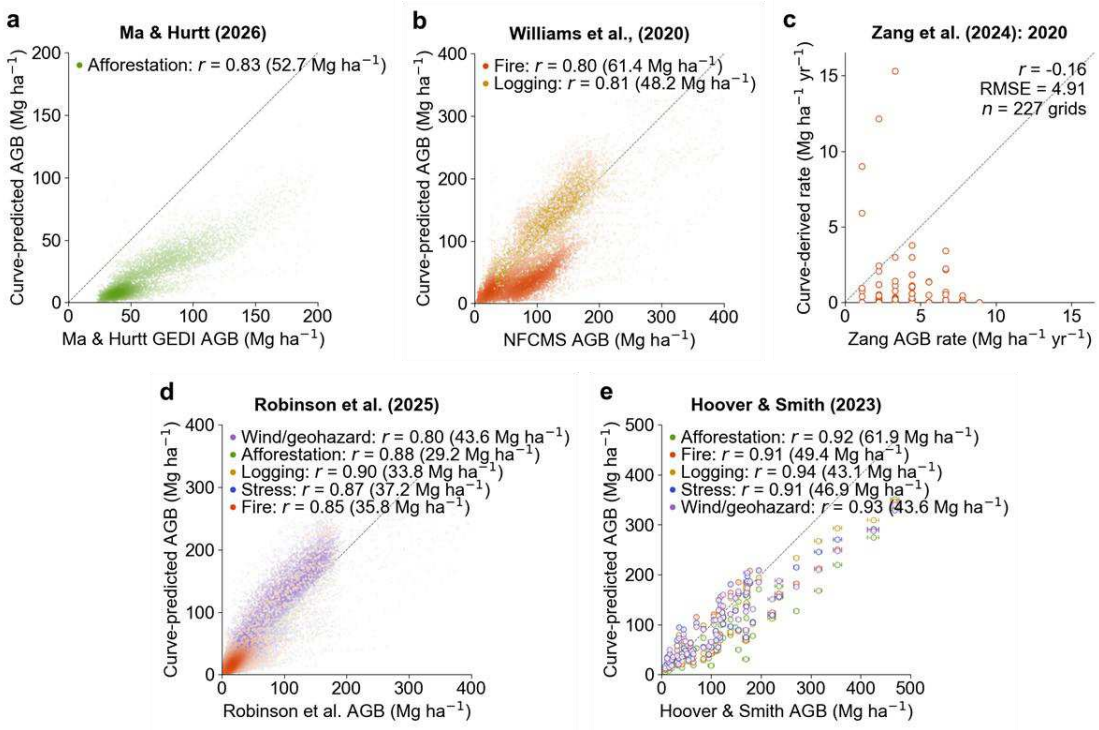


Figure 6. Intercomparison of CONUS-RecoveryCurves fitted using FIA-corrected AGB with published datasets. a, Afforestation curves compared with GEDI AGB from Ma and Hurtt (2026). **b**, Fire and logging curves compared with NFCMS AGB (Williams et al., 2020)**. c,** Curve-derived AGB regrowth rates for 2020 compared with Zang et al. (2024), using median rates over common valid pixels with positive rates in both products within each 1° grid cell. **d**, Five category-specific curves compared with AGB estimates from Robinson et al. (2025). **e**, Five category-specific curves compared with Hoover and Smith (2023) regional age-class AGB. Dashed lines indicate the 1:1

relationship. In-panel annotations report Pearson's correlation coefficient (*r*), with RMSE values shown in parentheses (Mg ha^{-1} for **a**, **b**, **d**, and **e**; Mg ha^{-1} yr^{-1} for **c**). Corresponding comparisons using recovery curves fitted with original ESA CCI AGB are presented in **Figure S7**.

4.5 Sensitivity of recovery estimates

Sensitivity analyses showed that the three recovery metrics responded differently to AGB calibration and selection of the 200-year reference point (**Fig. 7**). Relative to the baseline using FIA-corrected AGB and the 85th-percentile 200-year reference point, the configuration using the original ESA CCI AGB with the same reference point specification produced substantially higher median *initial AGB* for fire, wind/geohazard, stress, and logging (36.0% to 60.2%), but a modest decrease for afforestation (-5.2%). The higher *initial AGB* estimates are consistent with the tendency of original CCI AGB to overestimate biomass in young, low-biomass forests relative to FIA observations (**Figure S1**). The effects on *R30* were strongly category dependent, ranging from a 69.5% decrease for fire to a 67.9% increase for afforestation, whereas the effects on AGB_{max} were comparatively small (-10.0% to 4.8%). The choice of reference point percentile primarily affected AGB_{max}: relative to the 85th-percentile reference, the 75th-percentile reference reduced category-level median AGB_{max} by 4.2% to 7.2%, whereas the 95th-percentile reference increased it by 11.7%–16.7%. *Initial AGB* and *R30* were less sensitive to reference point selection, with changes remaining within approximately 7% across all categories. This pattern is consistent with the 200-year reference point primarily constraining the late-stage biomass level rather than the initial biomass.

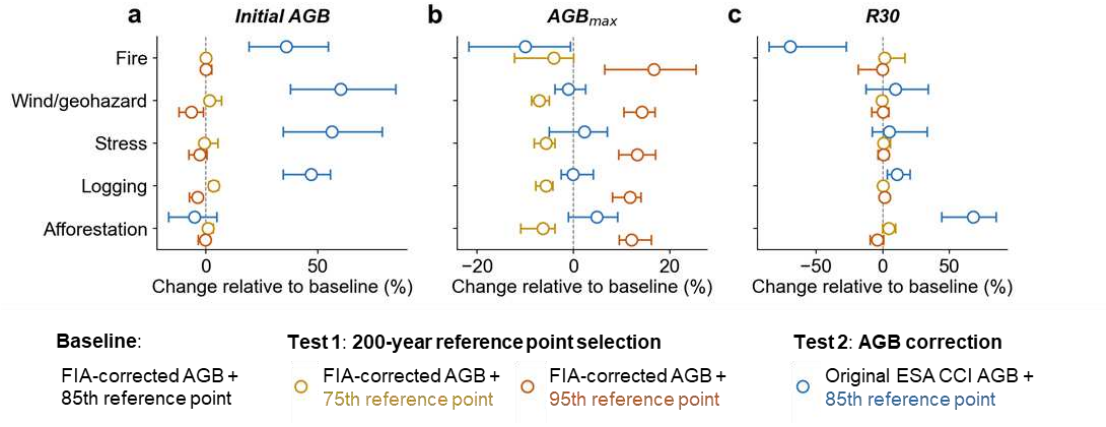


Figure 7. Sensitivity of recovery metrics relative to the reference configuration based on FIA-corrected AGB and the 85th-percentile 200-year reference point. **a-c**, Relative changes in category-level median *initial AGB*, AGB_{max}, and *R30*, respectively. Symbols indicate changes under three alternative configurations: FIA-corrected AGB with the 75th-percentile reference point (Test S1, yellow), FIA-corrected AGB with the 95th-percentile reference point (Test S1, orange), and original ESA CCI AGB with the 85th-percentile reference point (Test S2, blue). Horizontal error bars represent paired-grid bootstrap 95% intervals. Only grid cells with valid direct fits in the corresponding configurations were included; nearest-neighbor gap-filled estimates were excluded.

5. Usage notes

CONUS-RecoveryCurves is intended to support regional- to national-scale assessments of forest biomass recovery and associated carbon accumulation (Cook-Patton et al., 2020; Robinson et al., 2025), and to provide empirical constraints for evaluating and calibrating biomass accumulation in terrestrial biosphere models (Wu et al., 2026b). Users are encouraged to use the FIA-corrected version as the primary product because it generally showed greater consistency with the reference datasets (**Figure 6**) than the version derived from original ESA CCI AGB (**Figure S7**). The original-AGB version is also provided for sensitivity analysis. Curve parameters and derived metrics should be used together with the accompanying quality layers. Estimates from valid direct fits are preferable for analyses requiring locally constrained recovery dynamics. Gap-filled estimates extend spatial coverage by using parameters from the geographically nearest valid grid cell of the same category and may be less representative of local recovery conditions.

Despite the broad spatial coverage and category-specific information provided by CONUS-RecoveryCurves, several considerations are important when interpreting and applying the dataset. Differences among the category-specific curves should not be attributed solely to disturbance or land-use-change type, because the categories differ in their spatial distributions and environmental conditions, which can influence biomass accumulation during forest regrowth (Cook-Patton et al., 2020). Additional uncertainty arises from limitations in the Landsat disturbance record, LCMS land-cover changes, and GAMI forest-age estimates, which may affect the identification of recovery categories and recovery ages. Furthermore, the space-for-time approach assumes that spatial differences among forests of different recovery ages approximate temporal recovery (Walker et al., 2010). It therefore does not explicitly capture the effects of temporally varying factors, such as climate change, atmospheric CO_2 concentrations, and changes in forest management practices, on forest growth and recovery rates (Hogan et al., 2024).

6. Code availability

The Python code used to generate, quality-control, analyze, and visualize the CONUS-RecoveryCurves dataset is available from Nan Meng (nan.meng@lsce.ipsl.fr) upon reasonable request. The final version of the code will be deposited in a public repository upon publication.

Acknowledgements

P.C., acknowledge the support from the CALIPSO (Carbon Loss in Plant Soils and Oceans) project funded through the generosity of Schmidt Science. P.C. and N.M. thank the support from the European Space Agency Climate Change Initiative (ESA-CCI) RECCAP2-CS project (ESA ESRIN/4000144908/24/I-LR). This work was also supported by the ESA-CCI Biomass project (ESA ESRIN/4000123662/18/I-NB), the French National Research Agency (ANR) under the French–German AI4Forest project

(ANR-22-FAI1-0002-01), and the French National Research Agency (ANR) through the BOFOR project “Forest disturbances in the Russian boreal forest and their impact on carbon storage” (ANR-24-CE92-0048).

References

Bates, D.M., Watts, D.G. 1988. *Nonlinear Regression Analysis and Its Applications*. John Wiley & Sons, New York.

Besnard, S., Koirala, S., Santoro, M., Weber, U., Nelson, J., Gütter, J., Herault, B., Kassi, J., N'Guessan, A., Neigh, C., Poulter, B., Zhang, T., Carvalhais, N. 2021. Mapping global forest age from forest inventories, biomass and climate data. *Earth System Science Data*, **13**(10), 4881-4896.

Campbell, J.L., Fontaine, J.B., Donato, D.C. 2016. Carbon emissions from decomposition of fire-killed trees following a large wildfire in Oregon, United States. *Journal of Geophysical Research: Biogeosciences*, **121**(3), 718-730.

Cole, L.E.S., Bhagwat, S.A., Willis, K.J. 2014. Recovery and resilience of tropical forests after disturbance. *Nature Communications*, **5**(1), 3906.

Cook-Patton, S.C., Leavitt, S.M., Gibbs, D., Harris, N.L., Lister, K., Anderson-Teixeira, K.J., Briggs, R.D., Chazdon, R.L., Crowther, T.W., Ellis, P.W., Griscom, H.P., Herrmann, V., Holl, K.D., Houghton, R.A., Larrosa, C., Lomax, G., Lucas, R., Madsen, P., Malhi, Y., Paquette, A., Parker, J.D., Paul, K., Routh, D., Roxburgh, S., Saatchi, S., van den Hoogen, J., Walker, W.S., Wheeler, C.E., Wood, S.A., Xu, L., Griscom, B.W. 2020. Mapping carbon accumulation potential from global natural forest regrowth. *Nature*, **585**(7826), 545-550.

Costanza, J.K., Koch, F.H., Reeves, M., Potter, K.M., Schleeweis, K., Riitters, K., Anderson, S.M., Brooks, E.B., Coulston, J.W., Joyce, L.A., Nepal, P., Poulter, B., Prestemon, J.P., Varner, J.M., Walker, D.M. 2023. Disturbances to Forests and Rangelands. 5-1-5-55.

Domke, G.M., Oswalt, S.N., Walters, B.F., Morin, R.S. 2020. Tree planting has the potential to increase carbon sequestration capacity of forests in the United States. *Proceedings of the National Academy of Sciences*, **117**(40), 24649-24651.

Frolking, S., Palace, M.W., Clark, D.B., Chambers, J.Q., Shugart, H.H., Hurtt, G.C. 2009. Forest disturbance and recovery: A general review in the context of spaceborne remote sensing of impacts on aboveground biomass and canopy structure. *Journal of Geophysical Research: Biogeosciences*, **114**(G2).

Harris, N.L., Hagen, S.C., Saatchi, S.S., Pearson, T.R.H., Woodall, C.W., Domke, G.M., Braswell, B.H., Walters, B.F., Brown, S., Salas, W., Fore, A., Yu, Y. 2016. Attribution of net carbon change by disturbance type across forest lands of the conterminous United States. *Carbon Balance Manag*, **11**(1), 24.

Heinrich, V., Holcomb, A., Besnard, S., Requena Suarez, D., Cook-Patton, S., Bourgoin, C., Chazdon, R., Gibbs, D.A., Souza Mendes, F., McNicol, I., Wheeler, C., Silva-Junior, C.H.L., Amani, B.H.K., Bastin, J.-F., Besisa Nguba, T., Chen, N., Chen, H., Ciais, P., Dalagnol, R., Dou, X., Duan, Q., Gao, X., Goodarzi, A.N., Hérault, B., House, J., Lapola, D.M., Liang, M., Meng, Z., Nabuurs, G.-J., Poor,

E., Parsons, L., Reiche, J., Sitch, S., Valbuena, R., Welsink, A.-J., Wiltshire, S., Wu, C., Xu, Y., Zhao, J., Aragão, L., Herold, M. 2026. A meta-analysis of carbon losses and gains from tropical moist forest degradation and regeneration. *Science Advances*, **12**(27), eadz1923.

Hogan, J.A., Domke, G.M., Zhu, K., Johnson, D.J., Lichstein, J.W. 2024. Climate change determines the sign of productivity trends in US forests. *Proceedings of the National Academy of Sciences*, **121**(4).

Hoover, C.M., Smith, J.E. 2023. Aboveground live tree carbon stock and change in forests of conterminous United States: influence of stand age. *Carbon Balance Manag*, **18**(1), 7.

Liu, Z., Li, F. 2003. The generalized Chapman-Richards function and applications to tree and stand growth. *Journal of Forestry Research*, **14**(1), 19-26.

Ma, L., Hurtt, G. 2026. Remote Sensing-Derived Forest Regrowth Canopy Height, Biomass, and Age Across the Americas, Zenodo.

Oehlert, G.W. 1992. A Note on the Delta Method. *The American Statistician*, **46**(1), 27-29.

Qiu, S., Zhu, Z., Yang, X., Woodcock, C.E., Fahey, R.T., Stehman, S., Zhang, Y., Cullerton, M., Grinstead, A., Hong, F., Song, K., Suh, J.W., Li, T., Ren, W., Nemani, R.R. 2025. A shift from human-directed to undirected wild land disturbances in the USA. *Nature Geoscience*, **18**(10), 989-996.

Queally, N., Zheng, T., Ye, Z., Kovach, K.R., Pavlick, R., Shafron, E., Schneider, F.D., Townsend, P.A. 2025. Functional Traits From Imaging Spectroscopy Inform Patterns of Forest Mortality During Sierra Nevada Drought. *Glob Chang Biol*, **31**(5), e70246.

Robinson, N., Drever, C.R., Gibbs, D.A., Lister, K., Esquivel-Muelbert, A., Heinrich, V., Ciais, P., Silva-Junior, C.H.L., Liu, Z., Pugh, T.A.M., Saatchi, S., Xu, Y., Cook-Patton, S.C. 2025. Protect young secondary forests for optimum carbon removal. *Nature Climate Change*, **15**(7), 793-800.

Santoro, M., Cartus, O. 2025. ESA Biomass Climate Change Initiative (Biomass_cci): Global datasets of forest above-ground biomass for the years 2007, 2010, 2015, 2016, 2017, 2018, 2019, 2020, 2021 and 2022, v6.0, NERC EDS Centre for Environmental Data Analysis.

Smith, J.E., Heath, L.S., Skog, K.E., Birdsey, R.A. 2006. Methods for calculating forest ecosystem and harvested carbon with standard estimates for forest types of the United States. U.S. Department of Agriculture, Forest Service, Northeastern Research Station.

Walker, L.R., Wardle, D.A., Bardgett, R.D., Clarkson, B.D. 2010. The use of chronosequences in studies of ecological succession and soil development. *Journal of Ecology*, **98**(4), 725-736.

Wear, D.N., Greis, J.G. 2013. The Southern Forest Futures Project: Technical Report.

Williams, C.A., Collatz, G.J., Masek, J., Goward, S.N. 2012. Carbon consequences of forest disturbance and recovery across the conterminous United States. *Global Biogeochemical Cycles*, **26**(1).

Williams, C.A., Gu, H., MacLean, R., Masek, J.G., Collatz, G.J. 2016. Disturbance and

the carbon balance of US forests: A quantitative review of impacts from harvests, fires, insects, and droughts. *Global and Planetary Change*, **143**, 66-80.

Williams, C.A., Hasler, N., Gu, H., Zhou, Y. 2020. Forest Carbon Stocks and Fluxes from the NFCMS, Conterminous USA, 1990-2010. Version 2 ed, ORNL Distributed Active Archive Center.

Woodall, C.W., Walters, B.F., Coulston, J.W., D'Amato, A.W., Domke, G.M., Russell, M.B., Sowers, P.A. 2015. Monitoring Network Confirms Land Use Change is a Substantial Component of the Forest Carbon Sink in the eastern United States. *Scientific Reports*, **5**(1), 17028.

Wu, C., Badgley, G., Goulden, M.L., Randerson, J.T., Trugman, A.T., Wang, J.A., Yang, L., Acil, N., Cook-Patton, S.C., Cullenward, D., Davis, S.J., Williams, C.A., Anderegg, W.R.L. 2026a. Forest carbon protocols underestimate climate-driven carbon loss risks. *Nature*, **654**(8117), 107-113.

Wu, C., Coffield, S.R., Goulden, M.L., Randerson, J.T., Trugman, A.T., Anderegg, W.R.L. 2023. Uncertainty in US forest carbon storage potential due to climate risks. *Nature Geoscience*, **16**(5), 422-429.

Wu, J., Ciais, P., Huang, Y., Fang, J., Gentine, P., Xu, Y., Goll, D., Liu, F., Du, X., Ma, R., Meng, N., Han, M., Zang, J., Jiang, R., Li, W. 2026b. Constraining boreal carbon allocation and turnover by assimilating forest growth dynamics in a differentiable framework. *EGUsphere*, **2026**, 1-27.

Xu, Y., Ciais, P., Santoro, M., Bourgoin, C., Ritter, F., Pellissier-Tanon, A., Feng, Y., Zhou, C., He, G., Heinrich, V., Besnard, S., Robinson, N., Cook-Patton, S.C., Chave, J., Aragao, L.E.O.C., Ometto, J.P., Bowring, S.P.K., Fayad, I., Zhu, L., Su, Y., Wigneron, J.-P., Li, W. 2026. Small persistent humid forest clearings drive tropical forest biomass losses. *Nature*, **649**(8096), 375-380.

Zang, J., Qiu, F., Zhang, Y. 2024. A global dataset of forest regrowth following wildfires. *Scientific Data*, **11**(1), 1052.

Zhu, K., Zhang, J., Niu, S., Chu, C., Luo, Y. 2018. Limits to growth of forest biomass carbon sink under climate change. *Nature Communications*, **9**(1), 2709.

448 **Supplementary material**

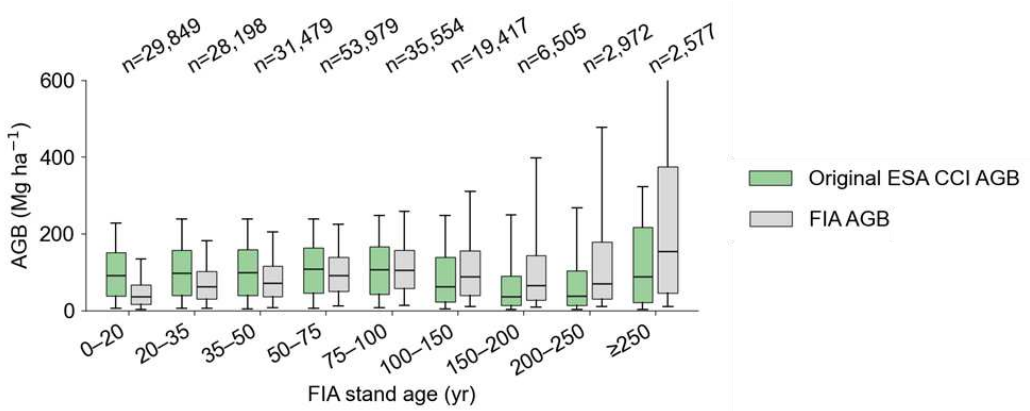
449 **Table S1. Performance and coverage of recovery curves fitted using original ESA**
450 **CCI AGB for five recovery categories**

Type	Median R^2 (IQR)	Median RMSE (IQR, Mg ha^{-1})	Accepted/eligible grids (%)
Fire	0.48 (0.31–0.66)	11.8 (5.4–25.7)	46.3
Wind/geohazard	0.48 (0.32–0.67)	28.8 (16.8–41.6)	43.6
Stress	0.39 (0.28–0.55)	20.9 (9.3–34.7)	42.3
Logging	0.74 (0.46–0.87)	11.7 (8.0–16.8)	67.0
Afforestation	0.95 (0.88–0.97)	4.8 (1.9–7.0)	56.6

451 **Table S2. Background information for the disturbance examples illustrated in**
452 **Figure 4c**.

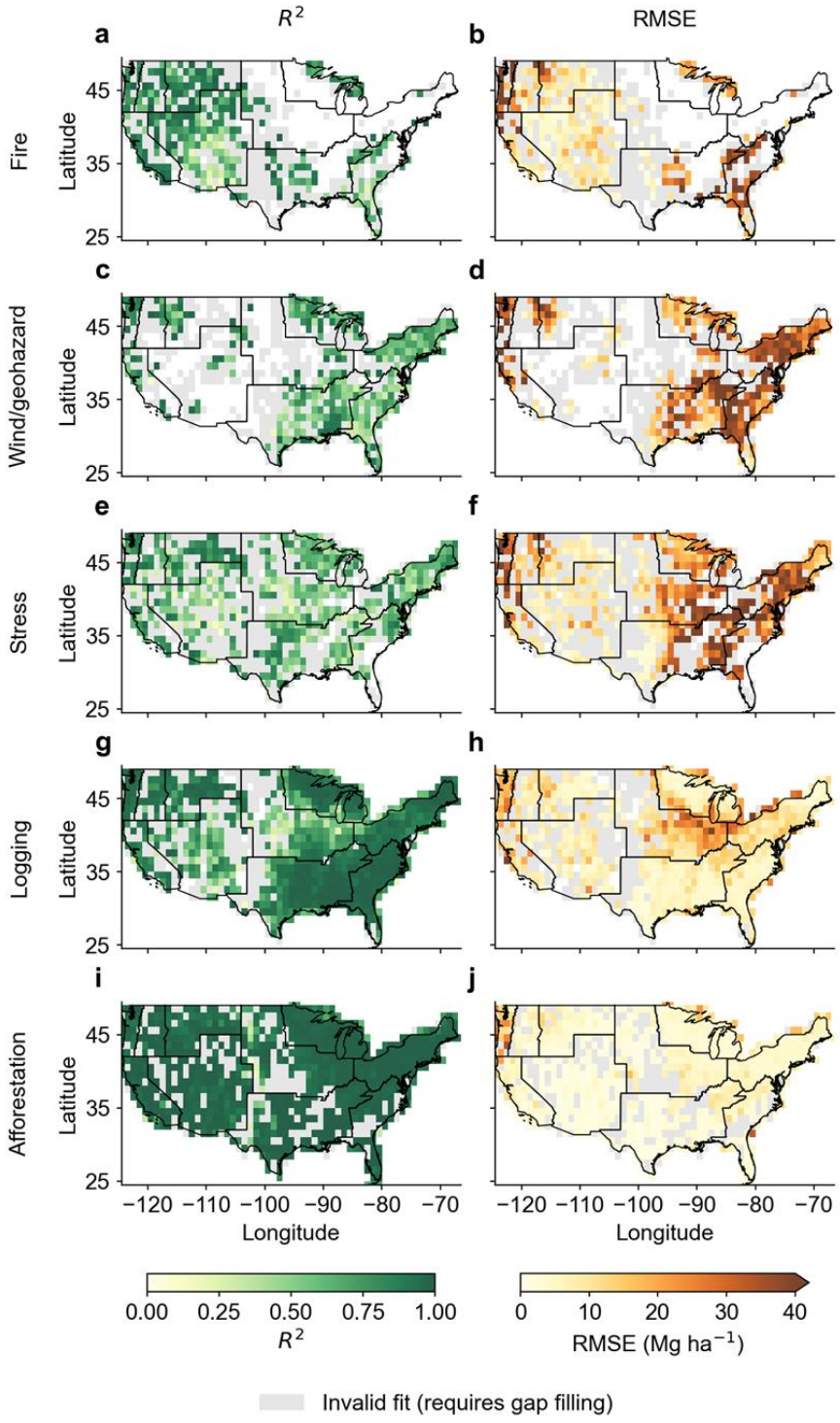
Disturbance type	Representative event	Region	Year	Reported extent or impact	Dominant forest type	References
Fire	Biscuit Fire	Oregon and Northern California	2002 (summer)	~0.2 Mha burned forest area	Mixed conifer forest	(Campbell et al., 2016)
Logging	Southeastern pine plantation harvest–regrowth cycle	Georgia, Alabama, and Mississippi	1990s–2010s	Extensive managed forest landscape	Loblolly pine plantation	(Wear & Greis, 2013)
Stress	Sierra Nevada drought mortality	Sierra Nevada, California	2012-2016	129 million trees died	Mixed conifer forest	(Queally et al., 2025)

453



454

455 **Figure S1. Comparison of original ESA CCI AGB and FIA AGB across forest-age**
456 **classes at matched FIA sites.**



457

458 **Figure S2. Spatial distributions of recovery-curve fitting performance using FIA-**
459 **corrected AGB**. R^2 (left) and RMSE (right) are shown for five recovery categories.
460 Fitting statistics are displayed only for valid direct fits; eligible grid cells failing the
461 fitting or plausibility criteria and therefore requiring gap filling are shown in grey.

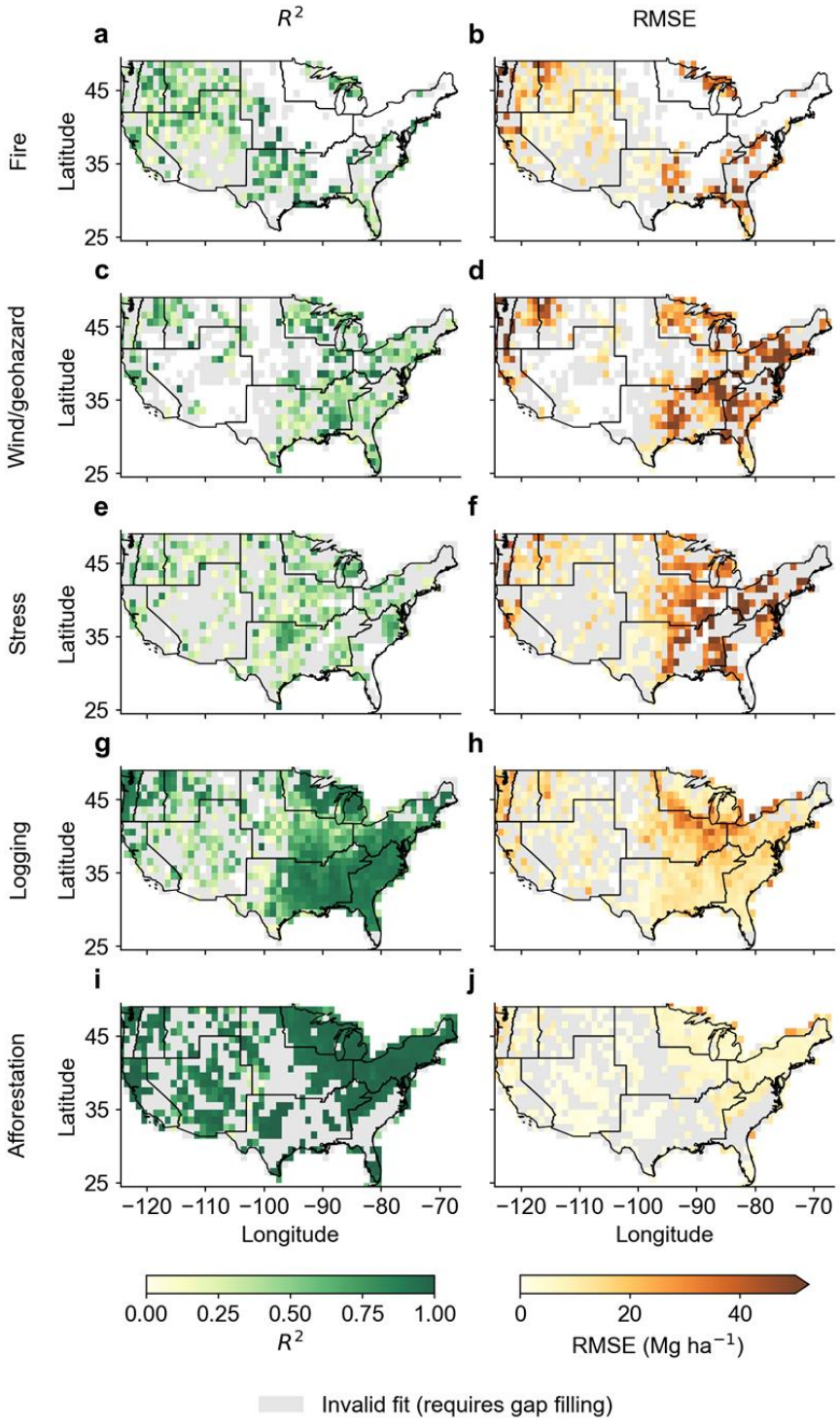


Figure S3. Spatial distributions of recovery-curve fitting performance using original ESA CCI AGB. R^2 (left) and RMSE (right) are shown for five recovery categories. Fitting statistics are displayed only for valid direct fits; eligible grid cells failing the fitting or plausibility criteria and therefore requiring gap filling are shown in grey.

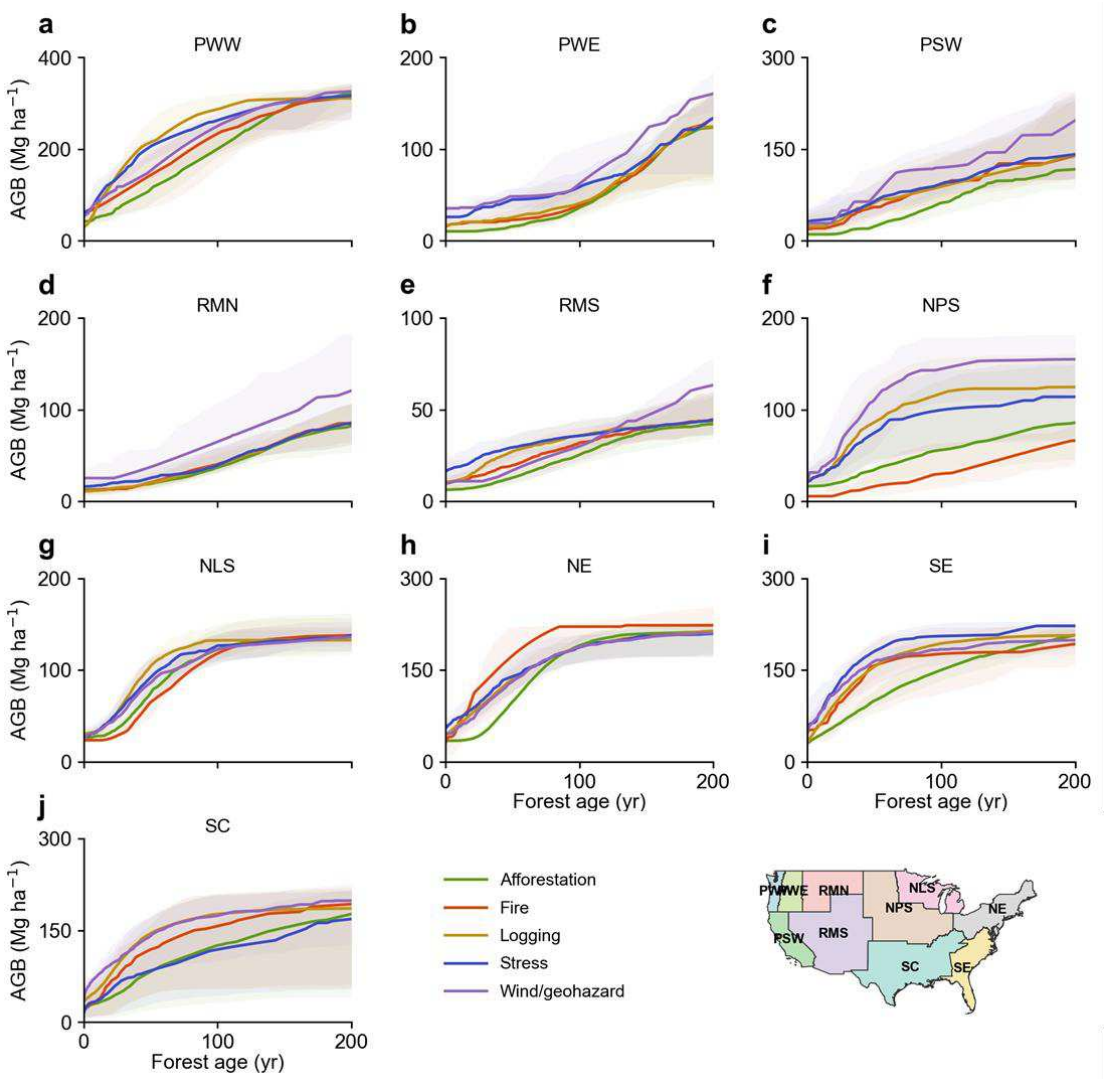


Figure S4. Regional recovery trajectories for five recovery categories based on FIA-corrected AGB. Each panel presents the median recovery trajectories for fire, wind/geohazard, stress, logging, and afforestation, within one subregion. Solid lines represent the pointwise median predictions from valid directly fitted 1° × 1° grid cells, and shading indicates the interquartile range among grid-cell predictions. The inset map shows the locations of the ten forest subregions defined by Smith et al. (2006). Regional abbreviations: PWW, Pacific Northwest, West; PWE, Pacific Northwest, East; PSW, Pacific Southwest; RMN, Rocky Mountain, North; RMS, Rocky Mountain, South; NPS, Northern Prairie States; NLS, Northern Lake States; NE, Northeast; SC, South Central; SE, Southeast.

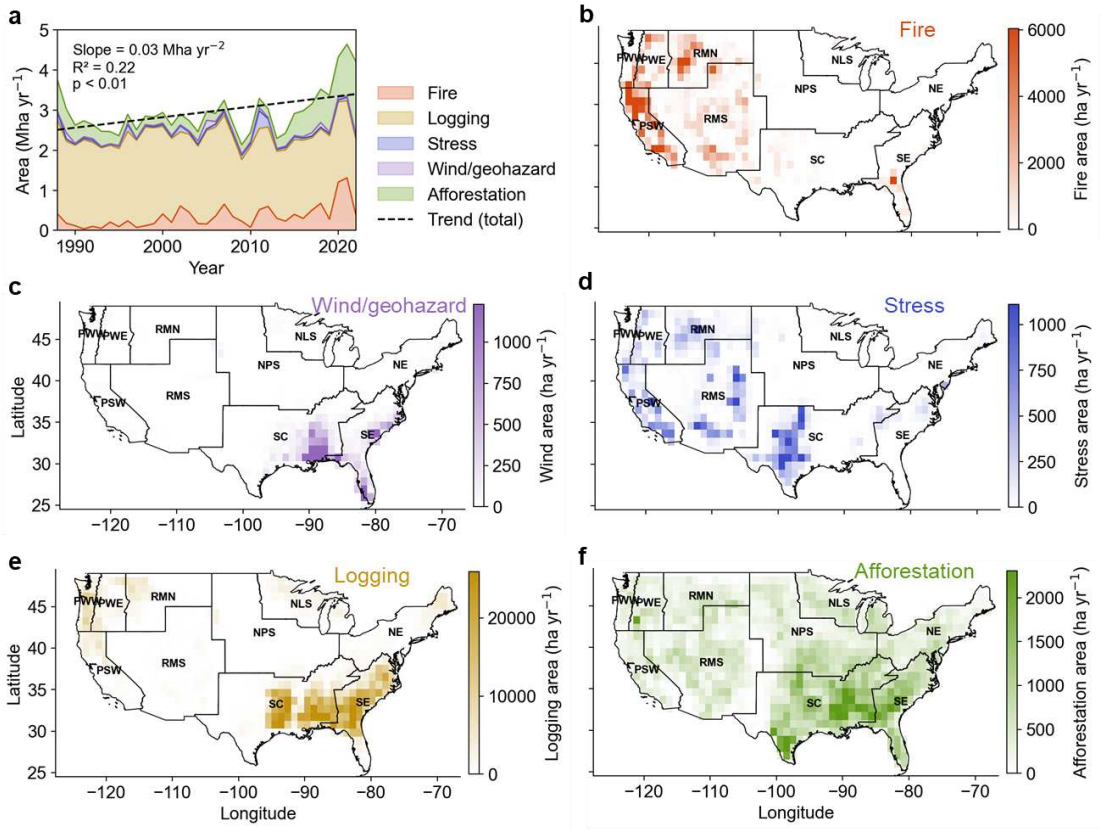


Figure S5. Temporal and spatial distributions of forest disturbance and afforestation categories across the CONUS. **a**, Annual areas of fire, wind/geohazard, stress, logging, and afforestation from 1988 to 2022. The dashed line represents the linear trend in the total annual area across the five categories. **b–f**, Spatial distributions of mean annual area for fire, wind/geohazard, stress, logging, and afforestation, respectively, summarized within 1° × 1° grid cells. Regional abbreviations: PWW, Pacific Northwest, West; PWE, Pacific Northwest, East; PSW, Pacific Southwest; RMN, Rocky Mountain, North; RMS, Rocky Mountain, South; NPS, Northern Prairie States; NLS, Northern Lake States; NE, Northeast; SC, South Central; SE, Southeast.

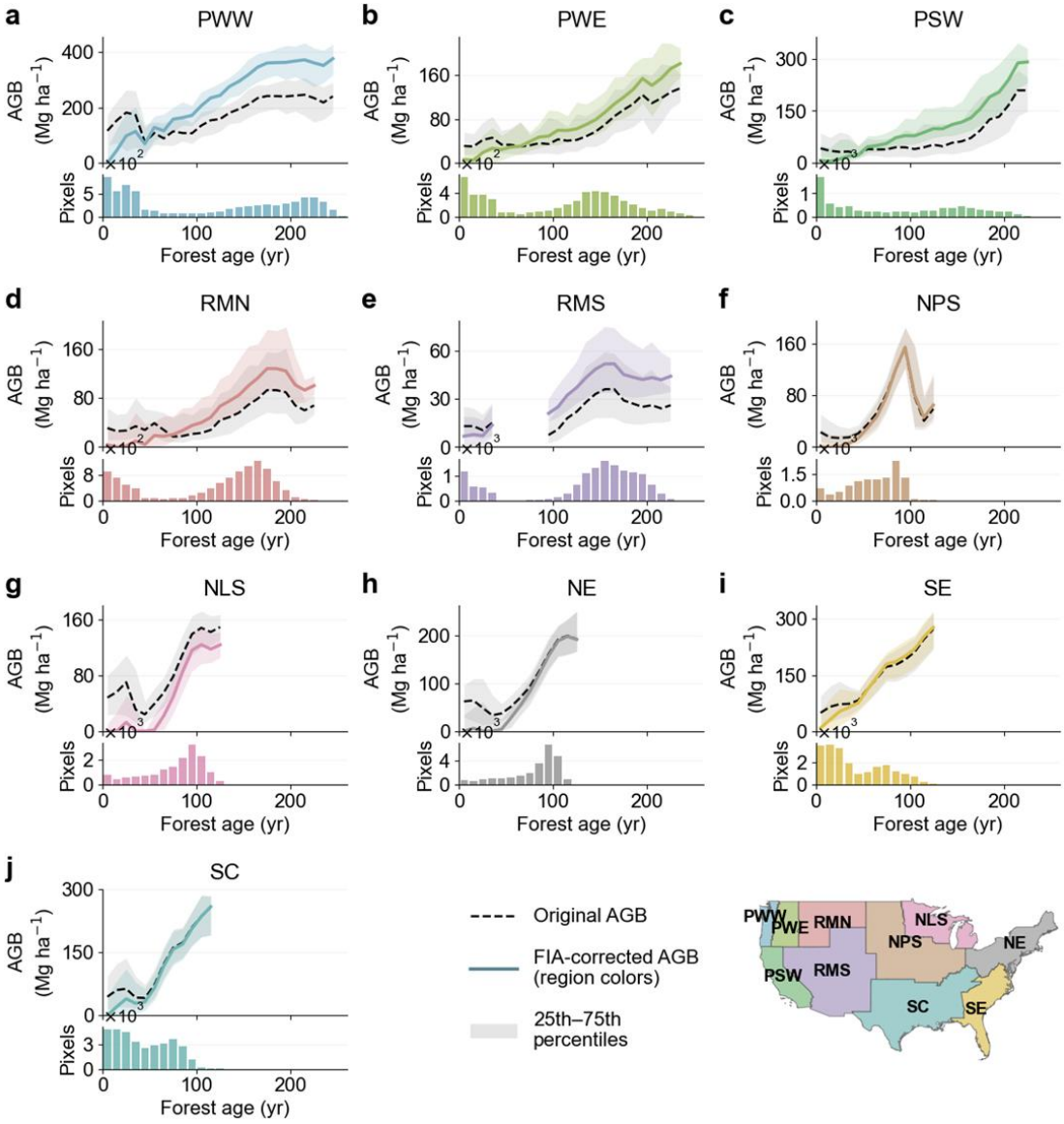


Figure S6. Regional age–AGB distributions before and after FIA-based bias correction. Green dashed and purple solid lines show median original and FIA-corrected AGB, respectively, within 10-year age classes for each forest region defined by Smith et al. (2006). Shading indicates the 25th–75th percentiles of sampled pixel-level AGB. Bars below each panel show the number of paired sample pixels in each age class. Medians and percentile ranges are displayed only for age classes containing at least 30 sample pixels. Regional abbreviations: PWW, Pacific Northwest, West; PWE, Pacific Northwest, East; PSW, Pacific Southwest; RMN, Rocky Mountain, North; RMS, Rocky Mountain, South; NPS, Northern Prairie States; NLS, Northern Lake States; NE, Northeast; SC, South Central; SE, Southeast.

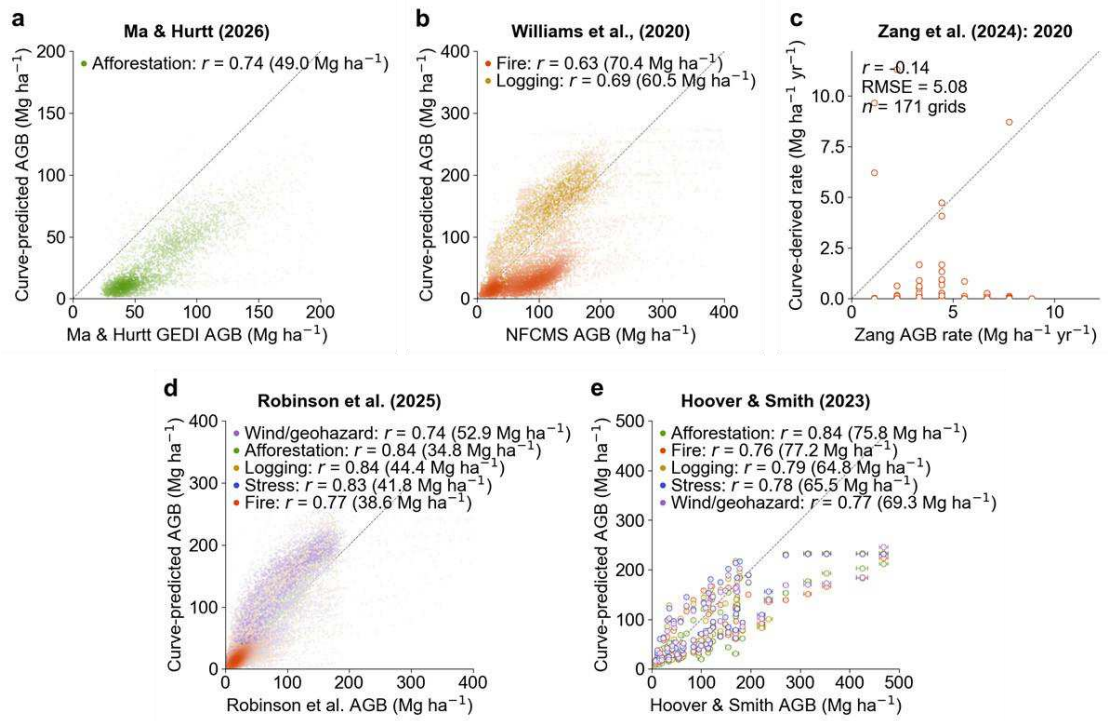


Figure S7. Intercomparison of CONUS-RecoveryCurves fitted using original ESA CCI AGB with published datasets. a, Afforestation curves compared with Ma and Hurtt (2026) GEDI AGB. **b**, Fire and logging curves compared with NFCMS AGB (Williams et al., 2020)**. c,** Curve-derived AGB regrowth rates for 2020 compared with Zang et al. (2024), using median rates over common valid pixels with positive rates in both products within each 1° grid cell. **d**, Five category-specific curves compared with Robinson et al. (2025) AGB estimates. **e**, Five category-specific curves compared with Hoover and Smith (2023) regional age-class AGB. Dashed lines indicate the 1:1 relationship. In-panel annotations report Pearson's correlation coefficient (*r*), with RMSE values shown in parentheses (Mg ha^{-1} for **a**, **b**, **d**, and **e**; Mg ha^{-1} yr^{-1} for **c**).